Alignment and momentum estimate evaluation for the CRIPT detector

Richard Hydomako

Prepared by:

Calian Ltd.
340 Legget Dr, Suite 101, Ottawa, Ontario, K2K 1Y6

Contract Number: W7714-4501094272
Contract Scientific Authority: David Waller, Defence Scientist, 613-998-9985

Contract Report
DRDC-RDDC-2015-C076
March 2015

Abstract

The Cosmic Ray Inspection and Passive Tomography (CRIPT) collaboration has constructed a large-scale detector prototype for investigating the use of comic ray muon scattering tomography for Special Nuclear Material (SNM) identification. In order to produce reconstructed images of the highest quality, it is important to ensure that the detector has achieved optimal performance. In this report, the software alignment of the scintillator bar positions is described. Additionally, the algorithm for estimating the momentum of individual cosmic-ray muons is described and evaluated using a detailed Monte Carlo simulation of the CRIPT detector.

This page intentionally left blank.

Table of contents

List of figures

List of tables

1 Introduction

The Cosmic Ray Inspection and Passive Tomography (CRIPT) project is an effort to construct a novel cosmic ray muon detector for the purposes of identifying Special Nuclear Material (SNM) [1, 2]. The CRIPT collaboration has constructed a large-scale prototype located at AECL's Chalk River facility for the purposes of investigating the merits of muon scattering tomography, wherein the three-dimensional density of a scanned object is inferred by the measured scattering of through-going charged particles. Extremely dense materials, such as SNM, can then be identified within the large three-dimensional scanning volume of the CRIPT detector.

1.1 Detector overview

The CRIPT detector (Fig. 1) is comprised of twelve 2m$\times$2m planes of triangular scintillator bars. Each plane contains 121 individual scintillator bars, which are 2m long and have a triangular cross-section with a base of 3.23 cm and height of 1.65 cm. The scintillator bars are arranged in a close-fitting pattern of alternating right-side-up and up-side-down bars such that there are no gaps across the plane surface. The scintillated light from each individual bar is collected by a wavelength-shifting optical fiber which is coupled to a 64-channel photo-multiplying tube (PMT) readout device (two PMTs are needed to read out each plane).

Furthermore, the CRIPT detector is divided into six layers, where each layer contains two planes arranged orthogonally. Two layers are located above the imaging volume and are referred to as the Upper Tracker (UT), two layers are located directly below the imaging volume and are referred to as the Lower Tracker (LT), and the final two layers are located below the LT and are referred to as the Spectrometer (SPEC). Note that this report is mainly focused on the optimization of the performance of the UT and LT layers, as these are layers are responsible for the tracking used for reconstructive imaging. The SPEC layers are largely ignored, as the multiple-scattering that occurs due to the steel plates (needed to perform the momentum estimate) inevitably degrades the overall SPEC performance.

2 Track-based alignment of the scintillator bar positions

Good knowledge of the physical positions of all of the scintillator bars within the CRIPT apparatus is needed to faithfully reconstruct cosmic-ray muon trajectories. However, even with measurements of the bar positions made during construction, it is often necessary to re-determine those positions, as positional shifting may occur during assembly. To this end, the actual collected cosmic-ray muon trajectory data is often useful in this alignment

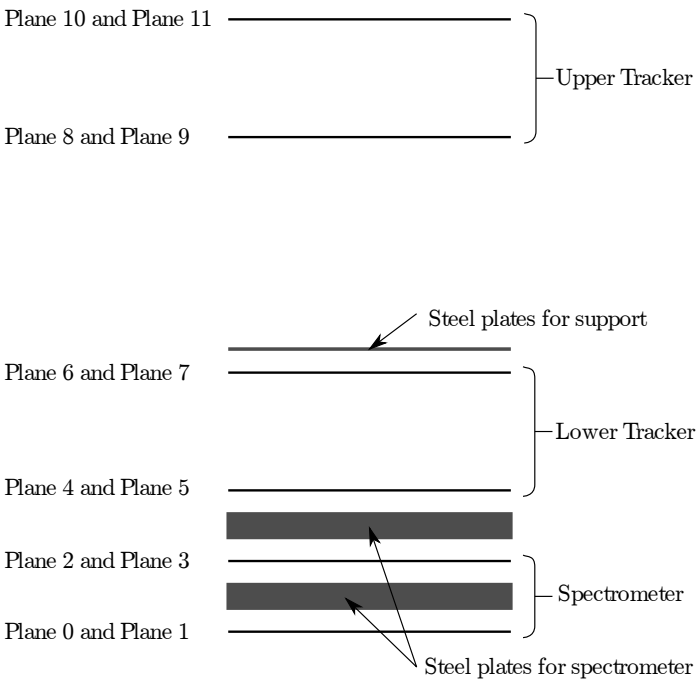

Figure 1: *Simplified diagram of the CRIPT detector, showing only the position of the scintillator layers and steel plates (not to scale).*

process. Following from the fact that multiple scattering from charged interactions have an angular distribution with zero mean, the overall average of all of the cosmic-ray muon tracks should follow a straight line through the detector. Since the expected distribution of cosmic-ray muons in known, we can compare the measured track distributions and look for any offsets that might indicate a discrepancies between the physical scintillator bar positions and the positions assumed in the software geometry.

2.1 Horizontal alignment

Since the planes of scintillator bars are on horizontal rails to facilitate their insertion into the apparatus, the horizontal degree of freedom has the fewest constraints (the vertical plane positions are constrained by the apparatus supports). Additionally, since the scintillator bars themselves are fairly well-constrained as a unit (double-sided tape was used on all sides of the bars to keep them fixed), the alignment procedure will be concerned only with the planes as a whole – any inter-bar alignment effects are ignored in this analysis.

The horizontal alignment procedure involves finding a set of plane displacements that minimize the objective function, χ^2:

$$\chi^2 = \sum_{i=0}^{n} \sum_{j=1}^{12} \left(\frac{x_{\text{Fit};i,j} - x_{\text{Measured};i,j}}{\sigma_j} \right)^2, \tag{1}$$

where i is the event number, n is the total number of events, $x_{\text{Measured};i,j}$ is the position of the hit candidate for the j-th plane in the frame of reference of that plane, $x_{\text{Fit};i,j}$ is the position in the frame of reference of the j-th plane found by a linear interpolation using the hit positions for the non-j planes, and σ_j is the hit position resolution for the j-th plane. It should be noted that in this formulation, the x and y contributions decouple and the alignment can be done separately for either direction. The minimization of Eq. 1 can then proceed using a function minimizer such as *Minuit* [3]. Using *Minuit*, the plane displacements are varied until a set of displacements that minimizes the overall sum of residuals is found. Figure 2 shows the residual distributions for all of the planes both before (black dotted histogram) and after (solid red histogram) the horizontal alignment procedure.

2.2 Vertical alignment

Displacements between the vertical positions of the physical planes and the vertical positions assumed in software can also be observed using the residual distributions described in Sec. 2.1. In this case, a misalignment in the vertical plane position translates into a non-zero slope of a residual distribution plot that is plotted as a function of hit position along the plane. Figure 3 shows a diagram explaining where the slop of the residual-position plot comes from: a vertically mis-aligned plane will systematically over- or under-estimate the residual values between the measured and fitted positions.

Likewise, Fig. 4 shows an example of the residual-position plots, along with the slope values determined through a linear fit. The goal of the vertical alignment procedure is then to adjust the vertical plane positions in software until the slopes converge to acceptable values. Intuitively, it might be expected that the expected slopes should be identically zero – however, the Monte Carlo simulation (whose geometry depicts a perfectly aligned detector) shows that small, non-zero, slopes are expected. These slopes are the result of fitting biases stemming from the multiple scattering of the muons, since the trajectories will depart from the linear approximation. To account for the scattering influence, the vertical plane positions are adjusted such that the residual-position slopes match the Monte Carlo simulation. This matching is done by first defining the following figure of merit, R:

$$R = \sum_{i=1}^{12} \left| m_i - m_{i;\text{MC}} \right|, \tag{2}$$

where m_i and $m_{i;\text{MC}}$ are the slopes of the residual-position plots for the i-th plane for the data and Monte Carlo simulation, respectively. By taking the absolute value of the term, R will reach a global minimum when the slopes of the distributions from the data match the slopes from the simulation.

Some simplifications can be made that allow for a 'by-hand' minimization of R. First, the inter-plane distance between the pairs of x and y planes is well-constrained by the apparatus

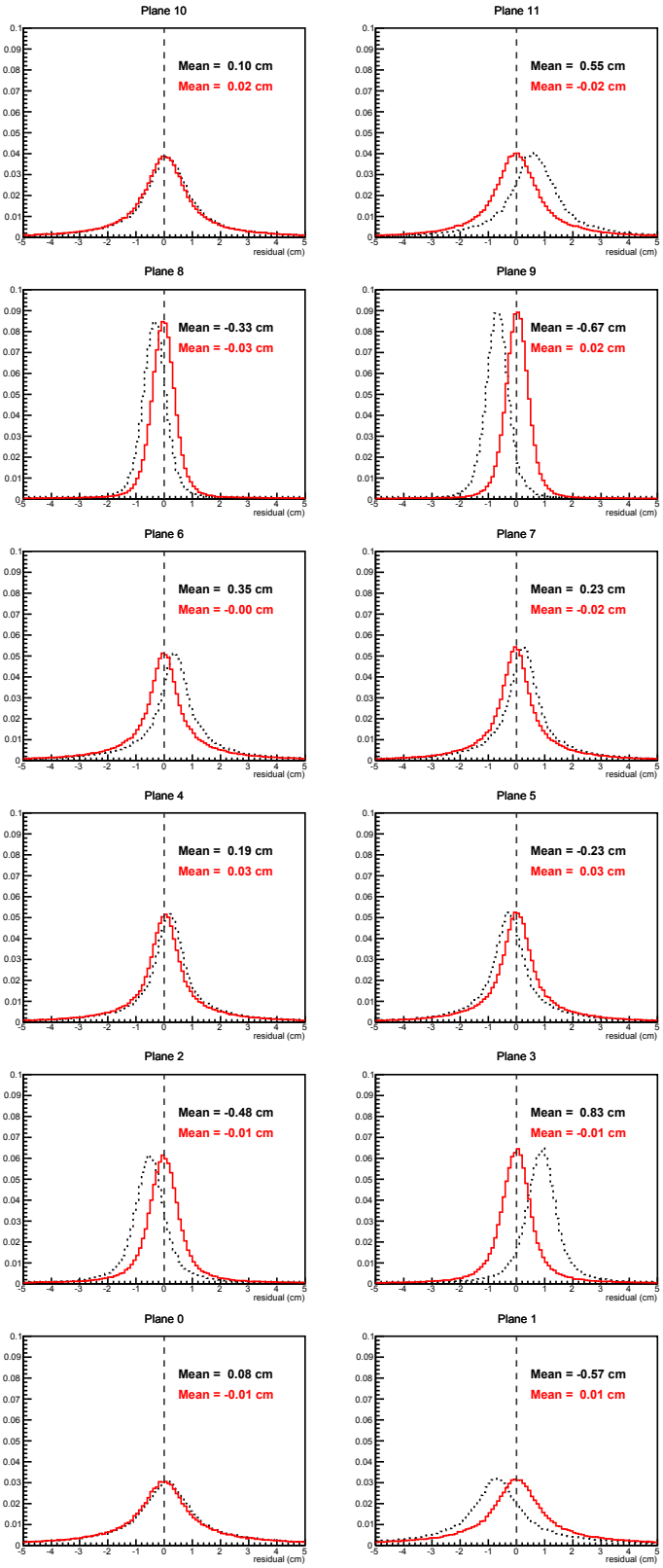

Figure 2: *Residual distributions before horizontal alignment procedure (black dotted trace) and after alignment procedure (red solid trace).*

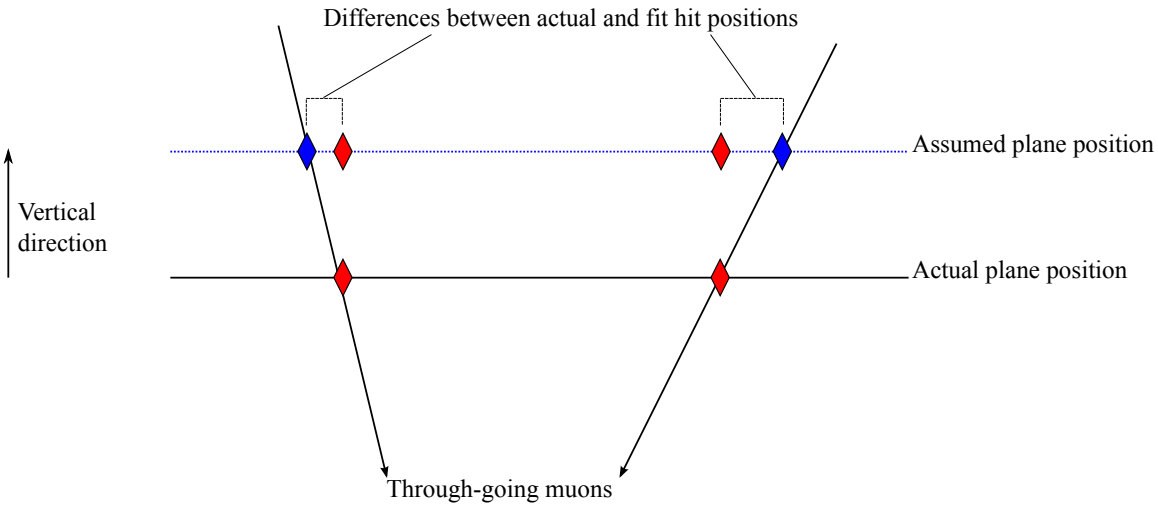

Figure 3: *Diagram of the effect of vertical misalignments. The long arrows depict the trajectories of the through-going muons, as well as the reconstructed trajectories found through a linear to the track hits. The red diamonds indicate the positions along the scintillator plane that the muon passed through, while the blue diamonds show how the reconstructed muon trajectory will systematically diverge from the actual hit positions for vertically misaligned planes.*

Step	Planes involved in position scan	Region being optimized
1	10-11	Upper tracker
2	6-7	Lower tracker
3	0-1	Spectrometer
4	8-9-10-11	UT with respect to LT
5	4-5-6-7-8-9-10-11	UT and LT with respect to SPEC

Table 1: *Step in the vertical alignment procedure. The vertical positions of all planes other than those listed are held fixed.*

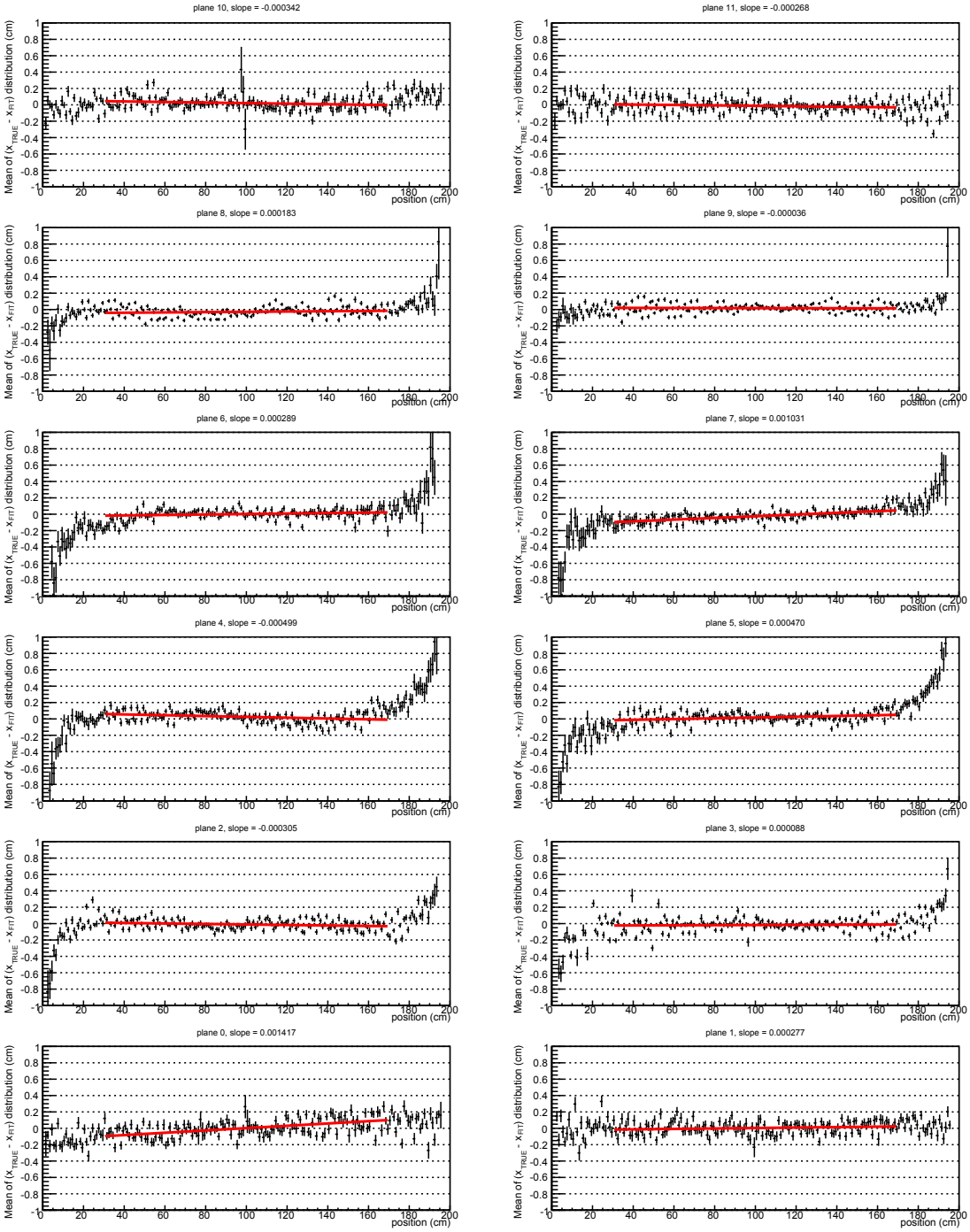

Figure 4: *Example residual-position plots, including the linear fits to determine the slopes of the plots. Each position bin gives the mean value of the residual distribution at that position.*

frame and is therefore assumed to be 1.7 cm for all of the pairs of planes. This assumption couples the positions of each of the $x-y$ pairs, which means that only the 6 positions of the coupled pairs need to be determined. Furthermore, by iteratively finding local minima for various combinations of planes, the overall minimum of R can be found. Table 1 describes the order in which to vary the planes (with all other planes held fixed) such that the region identified in the table is optimized. Figure 4 shows an example of the residual-position plots after the vertical alignment procedure has been applied.

3 Momentum estimate evaluation

The CRIPT apparatus contains a momentum spectrometer region that is specifically designed to estimate the cosmic-ray muon momentum on an event-by-event basis [1, 2]. The momentum estimate is a valuable piece of information that can be used to improve the scattering density estimate, and therefore improve the overall imaging and material identification. As such, it is important to understand the performance of the spectrometer and momentum estimate. This section will briefly outline the momentum estimation algorithm, and then evaluate its performance. It should be noted that the results presented here are primarily based on comparisons with the Monte Carlo simulation, since the momentum of the generated cosmic-ray muon is known and can be directly compared to the results determined from the estimate algorithm.

3.1 Reconstruction algorithm

As described in Sec. 1.1, the momentum spectrometer is comprised of two $x-y$ scintillator pair, interleaved with 10 cm thick iron plates (see Fig. 1). Since the iron plates have a known thickness and density, the expected width, θ_0, of the multiple scattering distribution for through-going cosmic-ray muons is described by the Molière formula [4]:

$$\theta_0 = \frac{13.6\ \text{MeV}}{\beta c p}\sqrt{x/X_{0,\text{Fe}}}\left[1+0.038\ln(x/X_{0,\text{Fe}})\right], \tag{3}$$

where $x/X_{0,\text{Fe}}$ is the thickness of the iron traversed in units of radiation length, βc is the velocity of the muon, and p is the muon momentum. Since the scattering depends inversely on the particle momentum, by measuring the amount of scatter that a cosmic-ray muon undergoes through a know thickness of iron, an estimate can be made for the muon momentum.

The estimate of the cosmic-ray muon momentum utilizes a Bayesian *maximum a posteriori* method, wherein a likelihood function along with a prior distribution are maximized to find a point-estimate of the muon momentum. That is, with a detector event with position

measurements $\vec{x}$, a model Θ can be constructed and the momentum can be estimated as

$$\begin{aligned}\hat{p} &= \arg\max_{p} f(\Theta|\tilde{\mathrm{x}}) \\ &\propto \arg\max_{p} f(\vec{x}|\Theta) g(\Theta),\end{aligned} \tag{4}$$

where $f(\Theta|\tilde{\mathrm{x}})$ is the posterior distribution, $f(\vec{x}|\Theta)$ is the likelihood function, and $g(\Theta)$ is the prior distribution. The proportionality in Eqn. 4 comes from a normalizing factor, which is left out here as it is unimportant for the maximization.

A detailed derivation of the likelihood function and the parameterizations of the probability density functions for the CRIPT spectrometer is given in Ref. [5], and summarized here as:

$$f(\vec{x}|\Theta) = \prod_{i\in \mathrm{LT,SPEC}} f(x_i - x_{m,i}) \prod_{i\in \mathrm{SPEC}} f(x_{m,i} - x_{m,i-1}|p_{i-1};\vec{\theta}_{i-1}) f(p_i|p_{i-1};\vec{\theta}_{i-1}), \tag{5}$$

where i indicates the scintillator plane, x_i gives the horizontal measurement, while $x_{m,i}$ gives the horizontal position of the model, $\vec{\theta}_i$ gives the track angle parameters. Furthermore, $f(x_i - x_{m,i})$ gives the probability density function representing the uncertainty in the model hit position, while $f(x_{m,i} - x_{m,i-1}|p_{i-1};\vec{\theta}_{i-1})$ and $f(p_i|p_{i-1};\vec{\theta}_{i-1})$ are the probability density functions for the expected muon scattering and momentum, given the momentum and track angles in the plane above. Since the expected scattering and momentum terms rely on values calculated from previous planes, the likelihood function has to be calculated in temporal order. That is, the expected scattering an momentum have to be calculated starting from the track angles determined in the LT, then proceeding to the top SPEC planes, then finally calculating the terms for the bottom SPEC planes.

The prior distribution in Eqn. 4 can be parameterized as

$$g(\Theta) = f(x_{0,m};\phi_0) f(p_0|x_0;\phi_0), \tag{6}$$

where $f(x_{0,m};\phi_0)$ and $f(p_0|x_0;\phi_0)$ are the probability distribution functions for the initial position and momentum, respectively, for the incoming cosmic-ray muons. The flux of cosmic-ray muons is generally uniform over length-scales similar to CRIPT detector, so setting the position term $f(x_{0,m};\phi_0) = 1$ simplifies the prior to be solely defined by the momentum distribution. The atmospheric cosmic-ray muon momentum distribution has been experimentally measured [6] and can be used as the prior distribution. A flat prior is also useful as it is found to have greater numeric stability in this case (when using a flat prior, the momentum estimate is equivalent to a maximum likelihood fit).

3.2 Estimated momentum reconstruction efficiency

The first aspect of the momentum estimate to investigate is the reconstruction efficiency. That is, how many events the algorithm will successfully process on average. Figure 5

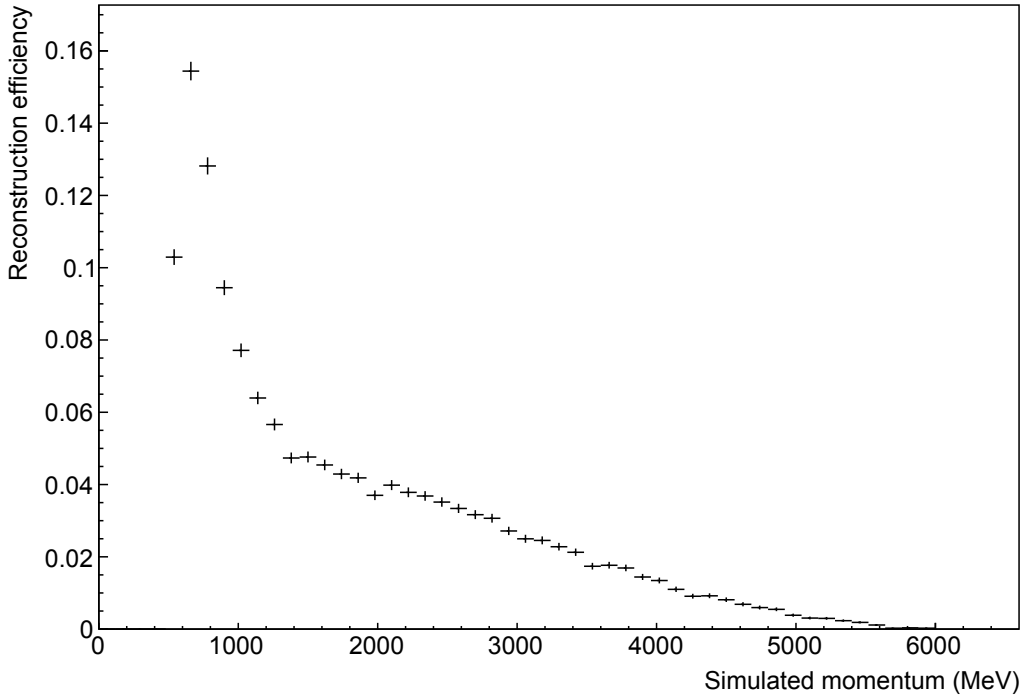

Figure 5: *The momentum reconstruction efficiency as a function of the simulated cosmic-ray muon momentum. Note that this efficiency is calculated with respect to the total number of simulated events, including those events that did not meet the acceptance of the spectrometer.*

shows the reconstruction efficiency as a function of the simulated cosmic-ray muon momentum. For this evaluation, cosmic-ray muon events were generated with momenta sampled from a uniform distribution between 0-6000 MeV and events for which a momentum value was successfully determined are binned according to the initial simulated muon momentum. It is clear from Fig. 5 that the momentum reconstruction is most effective between the range of about 500-1500 MeV. Below about 500 MeV, the cosmic-ray muons are not able to make it through all of the iron slabs, while above about 1500 MeV, there is not enough scattering to be reliably determined by the spectrometer planes. It should be noted that the results in Fig. 5 are normalized to the total number of simulated events for each momentum bin, such that the resultant efficiency is convoluted with the geometric acceptance of the spectrometer (whose planes were not forced by the trigger condition to be present in every event).

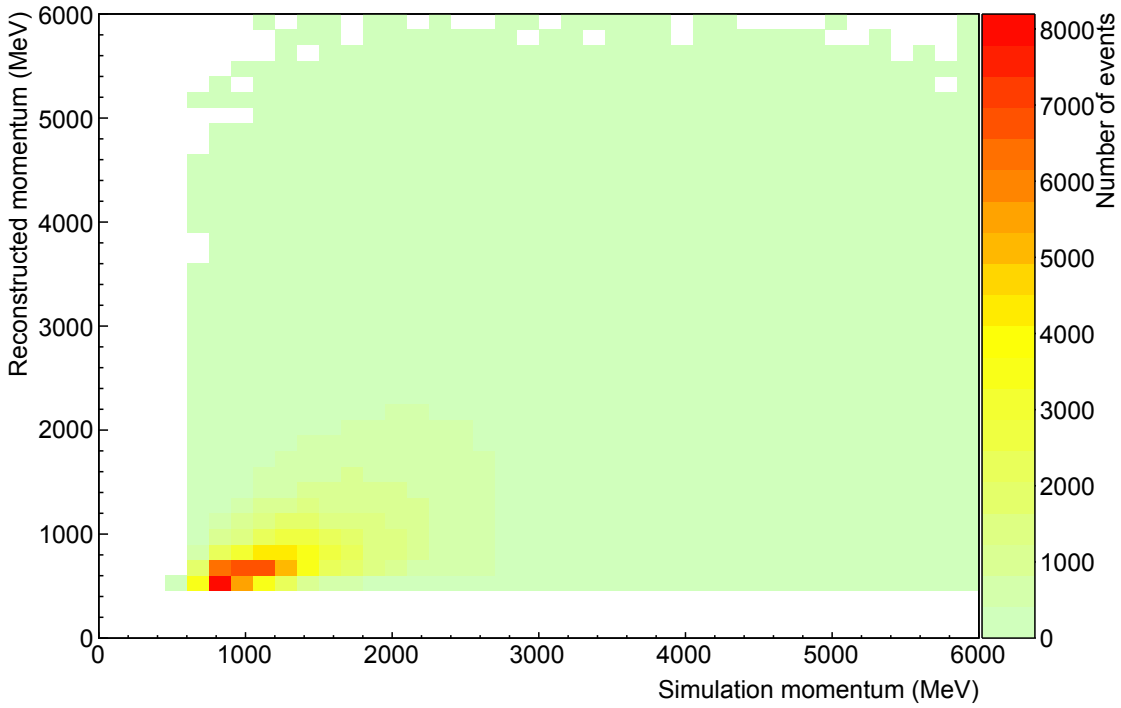

Figure 6: *Heatmap showing the correspondence between the simulated cosmic-ray muon momentum and the resulting reconstructed momentum.*

3.3 Correlation between generated and reconstructed momenta

Figure 6 gives a two-dimensional histogram that shows the estimated momentum with respect to the generated muon momentum. This plot demonstrates the correlation between the generated and reconstructed cosmic-ray muon momenta, which gives confidence towards the applicability of the momentum estimate, at least for the range of muon momenta highlighted in Sec. 3.2. The Pearson correlation coefficient for the simulated-reconstructed relationship is 0.51, which indicates a moderate correlation between the simulated and reconstructed momenta.

3.4 Reconstructed momentum resolution

The last evaluation metric to consider is the overall estimated momentum resolution. Here, the resolution is defined as the width of the $(P_{\text{reconstructed}} - P_{\text{simulated}})/P_{\text{simulated}}$ distribution. Figure 7 shows the resolution distribution along with a Gaussian fit to the central peak, which returns a mean of 37% and a width of 31%. The non-zero mean shows that the estimation algorithm systematically underestimates the muon momentum, although it is

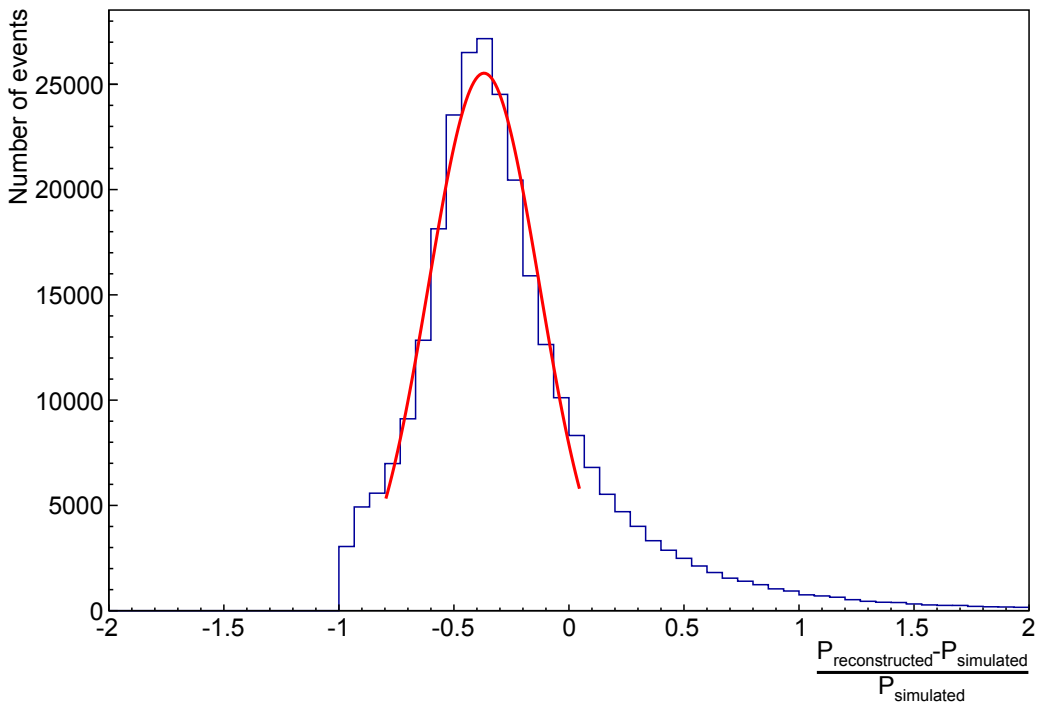

Figure 7: *The distribution of percent differences between simulated and reconstructed cosmic-ray muon momenta. The solid red curve shows a Gaussian fit to the central region of the distribution.*

possible that the mean offset could be mitigated using a global, or momentum-dependent, correction factor. However, the overall reconstructed momentum resolution is likely sufficient in order to improve the scattering density estimates.

4 Conclusion

This report outlined the procedure and results for the track-based software alignment of the CRIPT scintillator planes. Both the horizontal and vertical alignments were described. Additionally, an evaluation of the momentum estimation algorithm was given. Using a detailed Monte Carlo simulation to provide cosmic-ray muons events with known momentum, the reconstruction efficiency, correlation, and resolution of the momentum estimation algorithm were presented.

This page intentionally left blank.

References

[1] Waller, D. (2010), A simulation study of the Cosmic Ray Inspection and Passive Tomography (CRIPT) muon spectrometer, (DRDC Ottawa TM 2010-168) Defence R&D Canada – Ottawa.

[2] Waller, D. (2010), A simulation study of material discrimination using muon scattering tomography, (DRDC Ottawa TM 2010-211) Defence R&D Canada – Ottawa.

[3] James, F. (1994), MINUIT: Function Minimization and Error Analysis, Long Writeup D506, *CERN Program Library*.

[4] Beringer, J., Arguin, J. F., Barnett, R. M., Copic, K., Dahl, O., Groom, D. E., Lin, C. J., Lys, J., Murayama, H., Wohl, C. G., Yao, W. M., Zyla, P. A., Amsler, C., Antonelli, M., Asner, D. M., Baer, H., Band, H. R., Basaglia, T., Bauer, C. W., Beatty, J. J., Belousov, V. I., Bergren, E., Bernardi, G., Bertl, W., Bethke, S., Bichsel, H., Biebel, O., Blucher, E., Blusk, S., Brooijmans, G., Buchmueller, O., Cahn, R. N., Carena, M., Ceccucci, A., Chakraborty, D., Chen, M. C., Chivukula, R. S., Cowan, G., D'Ambrosio, G., Damour, T., de Florian, D., de Gouvêa, A., DeGrand, T., de Jong, P., Dissertori, G., Dobrescu, B., Doser, M., Drees, M., Edwards, D. A., Eidelman, S., Erler, J., Ezhela, V. V., Fetscher, W., Fields, B. D., Foster, B., Gaisser, T. K., Garren, L., Gerber, H. J., Gerbier, G., Gherghetta, T., Golwala, S., Goodman, M., Grab, C., Gritsan, A. V., Grivaz, J. F., Grünewald, M., Gurtu, A., Gutsche, T., Haber, H. E., Hagiwara, K., Hagmann, C., Hanhart, C., Hashimoto, S., Hayes, K. G., Heffner, M., Heltsley, B., Hernández-Rey, J. J., Hikasa, K., Höcker, A., Holder, J., Holtkamp, A., Huston, J., Jackson, J. D., Johnson, K. F., Junk, T., Karlen, D., Kirkby, D., Klein, S. R., Klempt, E., Kowalewski, R. V., Krauss, F., Kreps, M., Krusche, B., Kuyanov, Y. V., Kwon, Y., Lahav, O., Laiho, J., Langacker, P., Liddle, A., Ligeti, Z., Liss, T. M., Littenberg, L., Lugovsky, K. S., Lugovsky, S. B., Mannel, T., Manohar, A. V., Marciano, W. J., Martin, A. D., Masoni, A., Matthews, J., Milstead, D., Miquel, R., Mönig, K., Moortgat, F., Nakamura, K., Narain, M., Nason, P., Navas, S., Neubert, M., Nevski, P., Nir, Y., Olive, K. A., Pape, L., Parsons, J., Patrignani, C., Peacock, J. A., Petcov, S. T., Piepke, A., Pomarol, A., Punzi, G., Quadt, A., Raby, S., Raffelt, G., Ratcliff, B. N., Richardson, P., Roesler, S., Rolli, S., Romaniouk, A., Rosenberg, L. J., Rosner, J. L., Sachrajda, C. T., Sakai, Y., Salam, G. P., Sarkar, S., Sauli, F., Schneider, O., Scholberg, K., Scott, D., Seligman, W. G., Shaevitz, M. H., Sharpe, S. R., Silari, M., Sjöstrand, T., Skands, P., Smith, J. G., Smoot, G. F., Spanier, S., Spieler, H., Stahl, A., Stanev, T., Stone, S. L., Sumiyoshi, T., Syphers, M. J., Takahashi, F., Tanabashi, M., Terning, J., Titov, M., Tkachenko, N. P., Törnqvist, N. A., Tovey, D., Valencia, G., van Bibber, K., Venanzoni, G., Vincter, M. G., Vogel, P., Vogt, A., Walkowiak, W., Walter, C. W., Ward, D. R.,

Watari, T., Weiglein, G., Weinberg, E. J., Wiencke, L. R., Wolfenstein, L., Womersley, J., Woody, C. L., Workman, R. L., Yamamoto, A., Zeller, G. P., Zenin, O. V., Zhang, J., Zhu, R. Y., Harper, G., Lugovsky, V. S., and Schaffner, P. (2012), Review of Particle Physics, *Phys. Rev. D*, 86, 010001.

[5] Drouin, P.-L. and Waller, D. (2011), Muon momentum reconstruction algorithms for the CRIPT spectrometer, (DRDC Ottawa TM 2011-210) Defence R&D Canada – Ottawa.

[6] Motoki, M., Sanuki, T., Orito, S., Abe, K., Anraku, K., Asaoka, Y., Fujikawa, M., Fuke, H., Haino, S., Imori, M., Izumi, K., Maeno, T., Makida, Y., Matsui, N., Matsumoto, H., Matsunaga, H., Mitchell, J., Mitsui, T., Moiseev, A., Nishimura, J., Nozaki, M., Ormes, J., Saeki, T., Sasaki, M., Seo, E., Shikaze, Y., Sonoda, T., Streitmatter, R., Suzuki, J., Tanaka, K., Ueda, I., Wang, J., Yajima, N., Yamagami, T., Yamamoto, A., Yamamoto, Y., Yamato, K., Yoshida, T., and Yoshimura, K. (2003), Precise measurements of atmospheric muon fluxes with the BESS spectrometer, *Astroparticle Physics*, 19(1), 113 – 126.